

Space-time beams with tunable orbital group velocity for plasma superradiance

Gabrielle Vaz,^{1,2,3,*} Rafael Almeida,^{1,2,*} Pablo San Miguel Claveria,^{1,2,*} Robert Neumann,^{1,2} Joaquim Pereira,^{2,3} Carolina Miranda,^{2,3} Vincent Ginis,⁴ Jorge Vieira,^{1,2} Marta Fajardo,^{1,2} and Marco Piccardo^{2,3,†}

¹*GoLP/Instituto de Plasmas e Fusão Nuclear, Instituto Superior Técnico, Universidade de Lisboa, Lisbon, Portugal*

²*Department of Physics, Instituto Superior Técnico, Universidade de Lisboa, Lisbon, Portugal*

³*Instituto de Engenharia de Sistemas e Computadores – Microsistemas e Nanotecnologias (INESC MN) Lisbon, Portugal*

⁴*Data Analytics Lab, Vrije Universiteit Brussel, 1050 Brussel, Belgium*

(Dated: February 24, 2026)

Light springs are space-time beams that have a helical wavepacket. Due to this special property, light springs result into a rotating pulse when intercepting a plane lying orthogonal to their propagation direction. Associated to this, we introduce here the orbital group velocity, an additional tunable property of light springs. The orbital group velocity quantifies the speed of the light spring intensity rotation, distinctly from the conventional longitudinal group velocity, which describes the motion of the wavepacket envelope along its propagation axis. We demonstrate experimentally by tunable Fourier synthesis that the orbital group velocity can assume sub- and superluminal values, thus becoming a new platform for synthetic motion studies and control of laser-matter interactions. Particularly, in the superluminal regime, when interacting with a thin overdense plasma, we reveal by particle-in-cell simulations that the light spring unlocks superradiant radiation, due to the coherent excitation of the electrons in the plasma acting as a quasiparticle. This superradiant source inherits the ultrafast temporal dynamics of the light springs while emitting in the terahertz region, thus creating a new source of terahertz radiation controlled by the properties of spatiotemporal coupling of the laser. Therefore, spatiotemporal tuning of light springs is at the frontier of controlling laser-matter interaction and generating new tunable sources of radiation.

Space-time couplings appear in optical systems when the spectral properties of a beam depend on position, resulting in complex spatiotemporal correlations in the light field [1]. In ultrafast laser systems, these couplings were initially perceived as chromatic aberrations and often treated as a detrimental effect to be minimized [1, 2]. However, in recent years, beams with tunable spatiotemporal properties have been synthesized [3, 4] and are unlocking the possibility to explore new regimes of light-matter interaction [5] with applications in fields such as nonlinear conversion [6, 7] or quantum metrology [8]. This class of optical beams includes propagation-invariant laser pulses [9] and spatiotemporal optical vortices [10]. A particularly fascinating feature of spatiotemporal beams in pulsed laser systems is the possibility to tune the longitudinal velocity of the intensity peak, referred to as the group velocity (v_g), to values above the vacuum light speed c , without violating relativistic causality [11, 12], such as in the case of the flying-focus [13, 14].

Whereas these space-time correlations can result from misalignments in chromatic optics in the laser chain, synthesizing tunable space-time beams requires to realize the desired correlations between the spatial and temporal/frequency components in a coherent light pulse [12]. For this purpose, the use of advanced optical elements, such as flat optics, metasurfaces [15, 16] and spatial light modulators (SLMs) [17, 18], is playing a crucial role in the development of space-time beams and their applica-

tions. A new type of space-time beam synthesized thanks to these technologies is the light spring (LS). A LS has a helical wavepacket [19–22], which means that an ultrashort pulse is structured to create a spatiotemporal

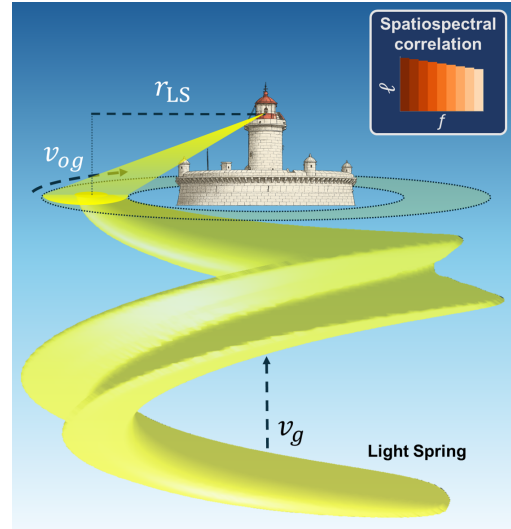


FIG. 1. The lighthouse effect in helical space-time beams. Connection between the apparent light motion observed in lighthouses and the orbital group velocity, v_{og} , in a light spring—a space-time coupled beam with a characteristic helical wavepacket. The maximum intensity of the wavepacket rotates at a tangential speed v_{og} on an intercepting plane, as the beam propagates with a longitudinal group velocity v_g . Similarly, the light emitted by a lighthouse produces the same pattern. ℓ represents the topological charge and f the laser frequency.

* These authors contributed equally to this work.

† marco.piccardo@tecnico.ulisboa.pt

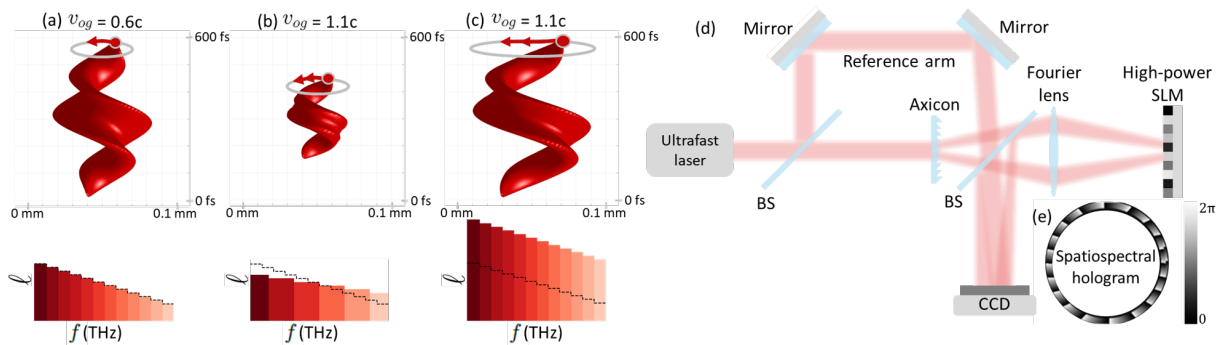


FIG. 2. **Tuning the orbital group velocity of light springs.** The orbital group velocity, v_{og} , tunability of a light spring can be accessed through control over the spatio-spectral correlation: by changing the slope of the linear relation—(a) to (b)—or by changing the average topological charge—(a) to (c). The control over the topological charges is experimentally achieved without any physical adjustments to the light spring generating setup (d), as it relies on changing the spatio-spectral hologram (e) displayed on the spatial light modulator. In (a), (b), and (c) f represents the laser frequency.

spring-like structure. This helical wavepacket results into an orbiting intensity profile when considering its intersection with a plane orthogonal to the LS propagation direction.

In this work we introduce the orbital group velocity, v_{og} , i.e., the velocity at which the peak intensity of a LS rotates, as a novel tunable degree of freedom of these spatiotemporal beams. We experimentally demonstrate its tunability to values below and above c . Moreover, we show via laser-plasma simulations how the ability to tune the v_{og} of the LS in a light-matter interaction scenario enables the generation of a superradiant plasma source with unprecedented properties for applications such as high-energy terahertz science.

Light springs are characterized by a linear correlation between the spectral components of an ultrafast laser pulse and the topological charge of their corresponding spatial modes. At a given plane perpendicular to the propagation of the laser pulse, a LS results in an orbiting intensity distribution around the propagation axis. We define the rotation speed of this intensity distribution, the orbital group velocity v_{og} , as

$$v_{og} = \frac{\partial \omega}{\partial \ell} r_{LS}, \quad (1)$$

where $\omega = 2\pi f$ and ℓ are the spectral angular frequency and topological charge of the LS, and r_{LS} is the radius of the rotating intensity maximum (see Suppl. Sec. IA for details on the equation). Equation 1 includes the slope of the spatio-spectral correlation, $\Omega = \partial \omega / \partial \ell$, which has the dimensions of an angular rotation rate, and multiplication by r_{LS} yields the tangential speed of the peak intensity. While Ω has been reported previously [19, 22], v_{og} —naturally compared to c —provides the appropriate figure of merit to quantify orbital motion and to identify new interaction regimes. Similarly to the well-known, widely-tunable v_g of space-time beams [11], we will demonstrate that this orbital motion can also be tailored to achieve sub- and superluminal values.

An interesting analogy of a LS can be found in the light emitted by a lighthouse (Fig. 1). In a lighthouse, the beam rotates with angular velocity $\dot{\alpha} = d\alpha/dt$ producing a moving spot at radius r_{LH} with tangential speed $v_{LH} = \dot{\alpha} r_{LH}$. For sufficiently large r_{LH} , v_{LH} can exceed c . This does not imply superluminal transport of energy or information as the spot is not a material entity, and the photons themselves propagate at light speed. Rather, successive photons illuminate successive positions. Similarly, a LS has a helical wavepacket, so that on a transverse plane its intensity maximum rotates with angular position $\alpha(t)$. The corresponding tangential speed is

$$v_{og} = \dot{\alpha} r_{LS}. \quad (2)$$

Thus, for a LS, Eq. 2 is equivalent to Eq. 1, and v_{og} quantifies the apparent motion [23–25] of the maximum intensity of the wavepacket, while no photon travels above c (see Suppl. Sec. IB).

Synthesizing a LS with an ultrashort laser pulse requires to control the topological charge of different spectral components of a laser pulse with orbital angular momentum (OAM). The experimental setup used to demonstrate the control over v_{og} can be seen in Fig. 2d. A titanium-sapphire laser (40 fs pulses at 1 kHz repetition rate from VOXEL high-intensity laser facility, see Suppl. Sec III) with a bandwidth of 13 THz was used to generate the LS. The ultrashort pulses reach an axicon grating (Suppl. Sec. II) [20], which diffracts different spectral components at different angles. Using a lens to conjugate the far field of the axicon, we generate a ring with a radially varying frequency distribution, where a reflective SLM is then used to impart an azimuthal phase with a radially varying topological charge, and thus generate the desired spatio-spectral correlation for the LS (Fig. 2e). The laser pulse with the imparted spatio-spectral coupling reflects off the SLM and is focused by the same conjugation lens to form the desired helical intensity distribution at the focal plane. As shown in Fig. 2d, a thin beamsplitter is used to separate the incoming laser pulse

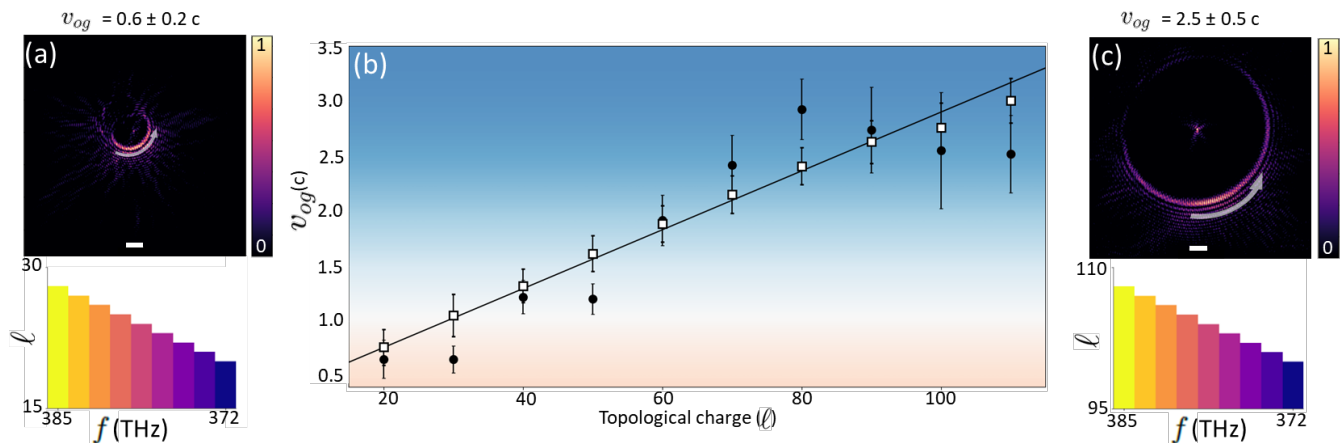


FIG. 3. **Experimental demonstration of subluminal to superluminal light springs.** Tunability of the orbital group velocity: the v_{og} can be experimentally modulated to achieve sub-(a) and superluminal (c) values via different spatio-spectral correlations. In (b) the white squares represent the programmed v_{og} (Eq. 1), while the black circles represent the experimentally measured v_{og} (Eq. 2), and the continuous line corresponds to numerical simulations of light springs. The scale bar in (a) and (c) is $173 \mu\text{m}$ and f represents the laser frequency.

from the LS before reaching the CMOS detector. This system is also known as a Fourier synthesizer, where the frequencies are spatially separated, and the OAM content is introduced via phase modulations.

Once the LS is synthesized, we reconstruct its intensity at the Fourier plane of the lens by measuring the interference of the LS with a reference pulse at this location. This reference pulse is taken from the incoming laser pulse with a beamsplitter placed prior to the axicon, after which it traverses an optical delay line to control its relative delay with respect to the LS at the measuring plane, where the detector is placed (Fig. 2e). Varying the relative delay between the LS and the reference pulse at the detector plane we can reconstruct the temporal evolution of the intensity distribution of the LS at this location [11]. This approach also allows us to characterize LS with different tunable parameters, such as different topological charges or a number of independent spectral radii (Suppl. Sec. III).

As prescribed by Eq. 1, there are two options to experimentally tune the v_{og} of a LS: either by tuning the slope of the spatio-spectral correlation or the radius of the LS. Figure 2a-c illustrates how to increase the v_{og} from $0.6c$ (Figure 2a) to $1.1c$ by either changing Ω (Figure 2b) or by enlarging the radius via an increase of the average topological charge (Figure 2c). In principle, changing any of these variables will give access to sub- and superluminal regimes of v_{og} values. However, experimentally, tuning v_{og} by controlling the slope of the spatio-spectral correlation limits the v_{og} range. The slope of the spatio-spectral correlation can be tuned by changing the frequency bandwidth used or the total variation of topological charge applied to create the LS (Eq. 1). Once a given experimental setup is built, the frequency bandwidth achieved by it is determined by the laser characteristics: decreasing it is

often detrimental, as it reduces the degrees of freedom in the Fourier synthesis of the space-time beam, while increasing it, typically requires complicated experimental setups that rely on nonlinear optics [26]. Alternatively, the control over the r_{LS} is simpler to implement experimentally, and also offers broader access to v_{og} regimes. This can be realized by either using a magnifying optical relay, or by changing the average topological charge of the LS [27]. The latter is the method used in this work to tune the v_{og} of the synthesized LS from subluminal to superluminal values, as it only requires changing the hologram applied at the SLM without any physical alterations to the experimental setup.

The orbital group velocity is set by the spatio-spectral correlation used to synthesize the LS (Eq. 1) and is therefore programmed through the hologram displayed on the SLM. To verify that the programmed orbital group velocity matches the actual v_{og} , we independently extract it by tracking the azimuthal angle of the intensity hotspot as the LS propagates (Eq. 2 and Suppl. Sec. IV). We also perform numerical simulations of the LS to benchmark the v_{og} tunability (Suppl. Sec. V). The simulated v_{og} are derived numerically, taking into account a Gaussian beam profile with a fixed waist and the same frequency bandwidth of the experimental laser pulse. Then the spatio-spectral correlation is imposed, and the resulting electromagnetic field is calculated assuming a superposition of Bessel-Gauss modes, created by an axicon grating (Suppl. Sec. V).

Fig. 3b exhibits a very good agreement between the simulated, programmed, and experimentally measured v_{og} . The programmed v_{og} relies on assuming that the axicon and SLM are creating the correlation that is given between the frequency bandwidth and the applied topological charges, which cannot be directly characterized and is

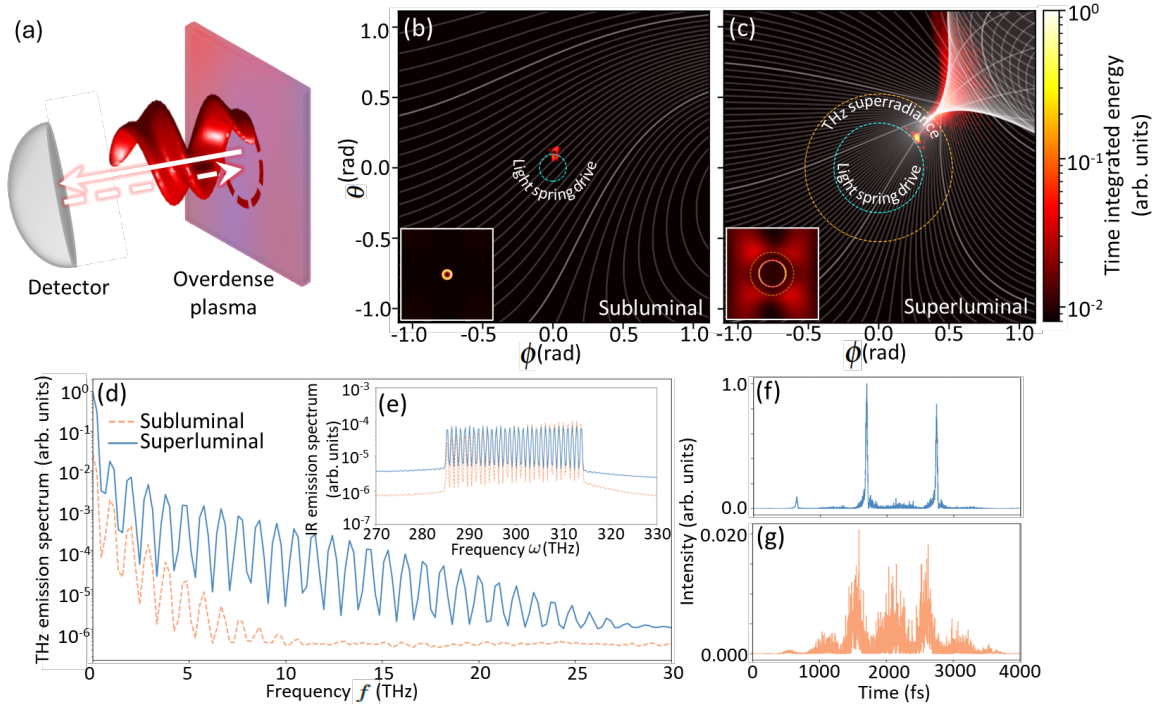


FIG. 4. **Superluminal light springs unlocking plasma superradiance.** A light spring (LS) reaches a thin overdense plasma, while a detector is placed collinearly to the LS to measure the radiation produced from the laser-plasma interaction (a). When the LS has a subluminal v_{og} (b), only the reflected LS and a few high harmonics are seen on the detector. However, when the v_{og} is superluminal, a strong enhancement in the emission signal and higher harmonics are measured at the detector (c). The presence of higher harmonics on the detector is directly related to the v_{og} regime of the LS (d), with (e) showing the reflected LS in the detector. Additionally, since the high harmonics appear only when the LS interacts with the plasma, the superradiance inherits the ultrafast temporal dynamics of the LS in the super- (f) and subluminal (g) case, with a nearly 50 \times peak signal enhancement in the former case. In (b) and (c), θ and ϕ represent the angle with respect to the z-y plane and the z-x plane, respectively. In (d) f represents the laser and superradiance frequencies.

only inferred by experimental setup characterization. On the other hand, the experimentally measured v_{og} is directly extracted from the LS intensity profile, depending only on the accuracy of the retrieval method. Even considering the inherent experimental errors, mainly coming from the pixel-size limitation imposed by the SLM and aberrations added in the optical path, it agrees well with the simulated and programmed v_{og} values, highlighting the robustness of this method in generating and controlling the LS properties, particularly the v_{og} . This shows that changing the topological charges used to create the LS, the v_{og} can be tuned from subluminal (Fig. 3a) to superluminal (Fig. 3c) values, demonstrating the wide tunability of the v_{og} .

The sub- and superluminal regimes of v_{og} unlock new control over light-matter interactions. Subluminal velocities are important when considering solid-state interactions [28] or laser-plasma accelerators [29, 30]. In these scenarios, coupling the v_{og} with gas jets or underdense plasmas can excite spatiotemporal structured plasma waves and control their motion, while enhancing particles' energy gain and trapping efficiency. Here, instead, we focus in superluminal velocities and show

by particle-in-cell simulations (Osiris [31]; Suppl. Sec. VI) and radiation diagnostics [32], that in an overdense plasma [33–35] the LS allows the control of the emitted radiation intensity, unlocking a superradiant effect based on superluminal [36] quasiparticles [37].

A quasiparticle is a localized nearly-constant current-density profile. Because it is a result of a collective effect, and unlike point-like particles (e.g., electrons), quasiparticles can execute arbitrary trajectories and travel at arbitrary speeds (even superluminal). The coherent part of the quasiparticle radiation spectrum is identical to that emitted by a single finite-sized particle undergoing a similar motion. The flexibility to control the quasiparticle motion opens new radiation mechanisms that are usually forbidden to single charged particles. For example, a quasiparticle traveling faster than c leads to quasiparticle Cherenkov radiation [36, 37]. Here, we propose to use a LS to unlock a novel superradiant effect based on a superluminal quasiparticle, traveling along a synchrotron (i.e. circular) trajectory in laser-matter interactions. The effect is due to the onset of an optical shock, which appears as a result of constructive interference of the radiation emitted by the quasiparticle during its trajectory, and at

the Cherenkov angle.

Fig. 4a portrays a schematic of our simulated setup. We consider subluminal and superluminal LS traveling along the z direction incident on a cold overdense plasma slab, perpendicular to the LS's direction. A virtual spherical detector is placed in the negative z -direction to detect the far field of the radiation emitted by the plasma electrons when interacting with the laser fields [32]. Fig. 4b and c display the instantaneous radiation intensity captured by the detector in the subluminal and superluminal regimes, respectively. The insets show the total integrated radiation intensity throughout the complete interaction. Both regimes include the pure reflection of the driver LS at the beam divergence angle $\theta_{BD} = \frac{\sqrt{\ell_0 \lambda_0}}{\sqrt{2\pi w_0}}$, where w_0 , ℓ_0 , and ω_0 are, respectively, the LS spot size, average topological charge, and main frequency (Suppl. Sec. VI). However, for the superluminal case (Fig. 4c), an extra intensity feature arises at the Cherenkov angle $\theta_{CH} = \sin^{-1}(c/v_{og})$. This definition of the Cherenkov angle differs from the standard $\cos^{-1}(c/v)$ as the geometry we tackle here is different: instead of linear, the trajectory of the quasiparticle is circular and thus creates an optical shock in a cardioid shape, whose cusp is at θ_{CH} . This shape arises from the intersection of the instantaneous wavefronts, which are plotted as white lines in Figs. 4b and c. A detailed description of these wavefronts is included in the Supplementary Sec. VII A.

Fig. 4d shows the low frequency part of the spectrum of the resulting radiation. It is composed of well defined peaks at harmonics of the frequency associated with the temporal pitch of the LS. For the superluminal case, the higher degree of coherence allows higher harmonics to appear, increasing the overall intensity of the signal. It is important to note that these harmonics are phase locked, thus effectively constituting a frequency comb with phase coherence inherited from the infrared LS laser drive, and have an azimuthal index corresponding to the harmonic order (Suppl. Sec. VII B). These characteristics are a direct consequence of the ultrafast spatiotemporal dynamics of the LS used. Fig. 4e portrays the radiation spectrum at the driver LS range showing that the intensity of the pure reflection is the same in both regimes. What is more, looking at a specific position on the detector (Fig. 4f and g), the electric field over time resembles a train of unipolar pulses spaced by the LS period of rotation (Suppl. Sec. VII C), whose intensity and contrast are much higher in the superluminal case. Regarding the efficiency of the process, without extensive optimization of the parameters, the energy of this train of pulses is $\approx 0.06\%$ of the energy of the LS drive in the superluminal regime (see Suppl. Sec. VII.D.), which is on par with [38, 39]. For the laser parameters considered here, the resulting pulsed radiation is in the terahertz range—a strategic region of the electromagnetic spectrum—and in the millijoule level, unlocking applications in structured

strong-field terahertz science [40, 41].

Therefore, the proper tuning of the v_{og} of the LS promises unprecedented control over laser-matter interactions at each v_{og} regime accessing new interaction scenarios, particularly suited for the acceleration of plasma to generate relativistic electron vortex beams [29] or as a tunable terahertz source of radiation, based on the Cherenkov mechanism. To experimentally measure such effects, it will be necessary to generate high-energy LS. Since the setup currently relies on an SLM, the energies that can be used to generate the LS are limited by it, but this problem could be circumvented by high-damage-threshold holograms fabricated in silica [42].

Additionally, when creating a LS, many parameters can be tuned, depending on how the axicon and holograms are generated. This opens the possibility to create LS with a radial gradient of v_{og} , precisely optimized to deliver different v_{og} at different radial positions, or by implementing the control of the LS chirp, to create a different frequency response based on the propagation of the LS. Lastly, as shown in this work, the generation of tunable space-time beams is currently at the frontier of unlocking new sources of radiation, while holding the promise to be the next generation of ultrafast light sources in strategic regions of the electromagnetic spectrum.

ACKNOWLEDGMENTS

The authors would like to thank Slava Smartsev and Jerome Faure for their involvement in the discussion of the techniques for light spring characterization. G.V. and M.P. received funding from the European Research Council (ERC StG) under the European Union's Horizon Europe research and innovation program (Grant agreement No. 101161858). M.P. wishes to acknowledge funding of the Research Unit INESC MN from the Fundação para a Ciência e a Tecnologia (FCT) through Plurianual financing (UIDB/05367/2025, UID/PRR/5367/2025 and UID/PRR2/05367/2025; DOI: 10.54499/UIS/PRR/05367/2025, 10.54499/UID/PRR2/05367/2025). The work of R.A. is supported by Fundação para a Ciência e Tecnologia (FCT, Portugal) grant number UI/BD/154677/2022 (DOI: 10.54499/UI/BD/154677/2022). This work was supported by FCT I.P. under Project 2024.07895.CPCA.A3 (DOI: 10.54499/2024.06987.CPCA.A3) at MareNostrum 5 supercomputer, jointly funded by EuroHPC JU, Portugal, Turkey and Spain, and under Project 2023.14906.PEX (DOI: 10.54499/2023.14906.PEX). PC, RN, and MF were funded by European Council Pathfinder Project 101047223, and LaserLab-Europe (grant agreement no. 871124).

-
- [1] S. W. Jolly, O. Gobert, and F. Quéré, “Spatio-temporal characterization of ultrashort laser beams: a tutorial,” *Journal of Optics* **22**, 103501 (2020).
- [2] D. Brinks, R. Hildner, F. D. Stefani, and N. F. van Hulst, “Beating spatio-temporal coupling: implications for pulse shaping and coherent control experiments,” *Optics Express* **19**, 26486 (2011).
- [3] Y. Shen *et al.*, “Roadmap on spatiotemporal light fields,” *Journal of Optics* **25**, 093001 (2023).
- [4] D. Cruz-Delgado *et al.*, “Synthesis of ultrafast wavepackets with tailored spatiotemporal properties,” *Nature Photonics* (2022).
- [5] M. Piccardo *et al.*, “Roadmap on multimode light shaping,” *Journal of Optics* **24**, 013001 (2021).
- [6] A. de las Heras *et al.*, “Extreme-ultraviolet vector-vortex beams from high harmonic generation,” *Optica* **9**, 71 (2021).
- [7] L. Rego *et al.*, “Generation of extreme-ultraviolet beams with time-varying orbital angular momentum,” *Science* **364** (2019).
- [8] F. S. Roux, “Nonlinear interferometry in all spatiotemporal degrees of freedom,” *Phys. Rev. A* **105** (2022).
- [9] M. Yessenov, B. Bhaduri, H. E. Kondakci, and A. F. Abouraddy, “Classification of propagation-invariant space-time wave packets in free space: Theory and experiments,” *Phys. Rev. A* **99** (2019).
- [10] A. Bekshaev, “Spatiotemporal optical vortices: Principles of description and basic properties,” *APL Photonics* **9** (2024).
- [11] H. E. Kondakci and A. F. Abouraddy, “Optical space-time wave packets having arbitrary group velocities in free space,” *Nature Communications* **10** (2019).
- [12] M. Yessenov *et al.*, “Space-time wave packets,” *Advances in Optics and Photonics* **14**, 455 (2022).
- [13] D. H. Froula *et al.*, “Flying focus: Spatial and temporal control of intensity for laser-based applications,” *Physics of Plasmas* **26**, 032109 (2019).
- [14] A. M. V. *et al.*, “Programmable-trajectory ultrafast flying focus pulses,” *Optics Express* **31**, 31354 (2023).
- [15] A. M. Shaltout, V. M. Shalaev, and M. L. Brongersma, “Spatiotemporal light control with active metasurfaces,” *Science* **364** (2019).
- [16] L. Chen *et al.*, “Synthesizing ultrafast optical pulses with arbitrary spatiotemporal control,” *Science Advances* **8** (2022).
- [17] C. Rosales-Guzmán and A. Forbes, “How to shape light with spatial light modulators,” in *How to Shape Light with Spatial Light Modulators* (Springer, 2017), Chap. 4, pp. 11–30.
- [18] M. A. Romer, L. A. Hall, and A. F. Abouraddy, “Synthesis and characterization of space-time light sheets: a tutorial,” *Journal of Optics* (2024).
- [19] G. Pariente and F. Quéré, “Spatio-temporal light springs: extended encoding of orbital angular momentum in ultrashort pulses,” *Optics Letters* **40**, 2037 (2015).
- [20] M. Piccardo *et al.*, “Broadband control of topological-spectral correlations in space-time beams,” *Nature Photonics* **17**, 822–828 (2023).
- [21] M. de Oliveira and A. Ambrosio, “Subcycle modulation of light’s orbital angular momentum via a Fourier space-time transformation,” *Science Advances* **11** (2025).
- [22] Q. Lin *et al.*, “Direct space-time manipulation mechanism for spatio-temporal coupling of ultrafast light field,” *Nature Communications* **15** (2024).
- [23] A. C. Harwood *et al.*, “Space-time optical diffraction from synthetic motion,” *Nature Communications* **16** (2025).
- [24] F. Belgiorno *et al.*, “Quantum radiation from superluminal refractive-index perturbations,” *Phys. Rev. Lett.* **104**, 140403 (2010).
- [25] J. Sloan *et al.*, “Controlling two-photon emission from superluminal and accelerating index perturbations,” *Nature Physics* **18**, 67–74 (2021).
- [26] P. Agostini and L. F. DiMauro, “The physics of attosecond light pulses,” *Rep. Prog. Phys.* **67**, 813–855 (2004).
- [27] A. M. Yao and M. J. Padgett, “Orbital angular momentum: origins, behavior and applications,” *Advances in Optics and Photonics* **3**, 161 (2011).
- [28] T. Omatsu and S. R. Allam, “Structured light solid-state laser sources,” *Journal of Optics* **27**, 073001 (2025).
- [29] J. Vieira, J. T. Mendonça, and F. Quéré, “Optical control of the topology of laser-plasma accelerators,” *Phys. Rev. Lett.* **121** (2018).
- [30] J. Vieira *et al.*, “High orbital angular momentum harmonic generation,” *Phys. Rev. Lett.* **117**, 265001 (2016).
- [31] R. A. Fonseca *et al.*, “OSIRIS: A three-dimensional, fully relativistic particle-in-cell code for modeling plasma-based accelerators,” in *Computational Science — ICCS 2002*, edited by P. M. A. Sloot *et al.* (Springer, Berlin, Heidelberg, 2002), pp. 342–351.
- [32] M. Pardal *et al.*, “RaDiO: An efficient spatiotemporal radiation diagnostic for particle-in-cell codes,” *Computer Physics Communications* **285**, 108634 (2023).
- [33] R. Lichters, J. Meyer-ter Vehn, and A. Pukhov, “Short-pulse laser harmonics from oscillating plasma surfaces driven at relativistic intensity,” *Physics of Plasmas* **3**, 3425–3437 (1996).
- [34] A. Denoëud *et al.*, “Interaction of ultraintense laser vortices with plasma mirrors,” *Phys. Rev. Lett.* **118**, 033902 (2017).
- [35] A. Leblanc *et al.*, “Plasma holograms for ultrahigh-intensity optics,” *Nature Physics* **13**, 440–443 (2017).
- [36] J. Vieira *et al.*, “Generalized superradiance for producing broadband coherent radiation with transversely modulated arbitrarily diluted bunches,” *Nature Physics* **17**, 99–104 (2020).
- [37] B. Malaca *et al.*, “Coherence and superradiance from a plasma-based quasiparticle accelerator,” *Nature Photonics* **18**, 39–45 (2023).
- [38] D. Jang *et al.*, “Efficient terahertz and Brunel harmonic generation from air plasma via mid-infrared coherent control,” *Optica* **6**, 1338 (2019).
- [39] C. Tailliez *et al.*, “Terahertz pulse generation by two-color laser fields with circular polarization,” *New Journal of Physics* **22**, 103038 (2020).
- [40] T. Pak *et al.*, “Multi-millijoule terahertz emission from laser-wakefield-accelerated electrons,” *Light: Science & Applications* **12**, 37 (2023).
- [41] G. Liao *et al.*, “Multimillijoule coherent terahertz bursts from picosecond laser-irradiated metal foils,” *Proc. Natl. Acad. Sci. USA* **116**, 3994–3999 (2019).

[42] B. Oliveira *et al.*, “High-aspect-ratio, ultratall silica meta-optics for high-intensity structured light,” *Optica* **12**, 713 (2025).

**SUPPLEMENTARY MATERIAL FOR:
SPACE-TIME BEAMS WITH TUNABLE ORBITAL GROUP VELOCITY FOR PLASMA
SUPERRADIANCE**

I. ORBITAL GROUP VELOCITY

In this work, the orbital group velocity (v_{og}) is introduced as a new tunable parameter for helical wavepackets. However, it can be related to known physical quantities and phenomena. In this section, we give the foundation of the definition of v_{og} , as well as briefly explore its connection with the lighthouse effect.

A. Definition of orbital group velocity

In cylindrical coordinates, an orbital angular momentum (OAM) mode can be written as

$$E(r, \phi, z) \sim A(r, z)e^{i\Phi(r, \phi, z)}, \Phi = kz + \ell\phi.$$

The local wavevector is

$$\mathbf{k}(r) = \nabla\Phi.$$

This becomes

$$\nabla\Phi = \hat{\mathbf{e}}_r \frac{\partial\Phi}{\partial r} + \hat{\mathbf{e}}_\phi \frac{1}{r} \frac{\partial\Phi}{\partial\phi} + \hat{\mathbf{e}}_z \frac{\partial\Phi}{\partial z}.$$

The azimuthal component is

$$k_\phi(r) = \frac{1}{r} \frac{\partial\Phi}{\partial\phi} = \frac{1}{r} \frac{\partial(\ell\phi)}{\partial\phi} = \frac{\ell}{r}.$$

The group velocity is typically written as $v_g = \frac{\partial\omega}{\partial k}$, thus we define its orbital counterpart in the azimuthal direction and at the hotspot radius $r = r_{LS}$ using the chain rule

$$\frac{\partial\omega}{\partial k_\phi} = \frac{\partial\omega}{\partial\ell} \cdot \frac{\partial\ell}{\partial k_\phi} = \frac{\partial\omega}{\partial\ell} \cdot r_{LS} = v_{og}.$$

B. Light spring and lighthouse relation

The lighthouse effect is a phenomenon that describes the apparent superluminal motion of the light source in a lighthouse. The lighthouse has a light source that is rotated with an angular velocity of $\frac{\partial\alpha(t)}{\partial t}$, which produces a moving spot at a given radius r_{LH} with linear velocity,

$$v_{LH} = \frac{\partial\alpha(t)}{\partial t} r_{LH}. \quad (1)$$

It can be easily seen that v_{LH} can assume arbitrarily large values. Particularly at a distant r_{LH} , it can exceed the velocity of light without breaking relativistic causality. For this case, the effect is a result of different locations being illuminated by different photons emitted at different times by the light source. On the other hand, in a given fixed orthogonal plane z , the light spring (LS) intensity hotspot describes a circular motion with linear velocity,

$$v_{og} = \frac{\partial\alpha(t)}{\partial t} r_{LS} \quad (2)$$

$$= \frac{\partial\omega}{\partial\ell} r_{LS}, \quad (3)$$

where r_{LS} , ω , and ℓ are the LS radius, angular frequency and topological charge, respectively. α is parameterized by the laboratory time on a fixed transverse plane. There is no break in relativistic causality. The superluminal motion observed arises from the angular arrival time of the photon, no energy or information is being transported. Therefore, the lighthouse spot and the LS intensity hotspot can be understood in the same way: in both cases one is observing an azimuthally evolving light pattern whose apparent transverse motion is set by how fast the pattern angle changes and by the radius at which it is observed. In this sense, the two systems share the same kinematic description of a rotating intensity pattern, even though the underlying physical mechanisms that generate the rotation are different.

II. AXICON DESIGN AND SPECIFICATIONS

The axicon used in this work is a multilevel axicon grating designed to implement, over each radial period, an approximate 0 to 2π phase ramp at the central wavelength of the titanium-sapphire source. The axicon has diameter $D = 10$ mm and radial period $d = 10$ μm . Each period is quantized into $N = 10$ phase levels. A master is fabricated by grayscale lithography, then the replica is fabricated in a UV-cured hybrid polymer (OrmoComp) using UV nanoimprint lithography. Ormocomp has a refractive index at the titanium-sapphire central wavelength of 1.51 and robustness similar to that of glass, making it suitable for operation with high-energy femtosecond pulses. A Gaussian beam with wavelength λ impinging on the axicon forms in the Fourier plane (reached using a lens with focal length f) a beam with annular radius given by

$$R(\lambda) \simeq f \frac{\lambda}{d}. \quad (4)$$

The beam waist w_0 of the input Gaussian sets the radial half-thickness of the focused annulus as

$$T(\lambda) \simeq \frac{f\lambda}{\pi w_0}. \quad (5)$$

The criterion for the number of independent spectral points in the design of an $\ell(f)$ correlation is that neighboring annuli do not overlap. Given our beam waist of $w_0 \sim 2.5$ mm and focal length $f = 75$ mm, we have around 10 independent spectral windows within the bandwidth of the titanium-sapphire laser for the synthesis of light spring' spatio-spectral correlations.

III. CHARACTERIZATION OF EXPERIMENTAL VARIABLES TO GENERATE LIGHT SPRINGS

The experiments were carried out in the VOXEL high-intensity laser facility at Instituto Superior Técnico, and as the light source, a titanium-sapphire laser (central wavelength of 800 nm), with nominal pulse energy of 3 mJ, beam-size at the output of 5 mm, and horizontal polarization.

To generate and reconstruct the LS, there are experimental variables that need to be optimized individually. Once the LS is synthesized, it is important to optimize the reconstruction. The technique used to reconstruct the LS in this work is off-axis digital holography (OADH) [1]. The most important parameter is properly adjusting the angle between the interferometer arm that has the LS and the reference arm. When using OADH, the amplitude and phase of the electromagnetic field are encoded on the first order of the fast Fourier transform (FFT) (Fig. 1a). Typically, the angle between the arms is maximized, so that the zero order does not add noise to the reconstruction. However, when reconstructing a LS, a bigger angle means a bigger tilt in the LS isosurface. To avoid this, the angle is set as small as possible, with the zero order of the FFT lying between the orders 1 and -1 (Fig. 1a).

Once the reconstruction of the LS is optimized (Fig. 1b and c), it is important to analyze how the axicon and spatial light modulator (SLM) are creating the LS. The axicon is designed to separate the frequencies of the laser in a first-order beam, with a radially-dispersed spectrum. The SLM is used to apply a topological charge to each one of the radii. To guarantee that the axicon and the SLM are giving the beam the desired properties, in addition to the topological charges, for the purpose of the characterization discussed in this section the hologram encodes an additional linear diffraction grating. The linear diffraction grating is applied such that each considered spectral window for the spatio-spectral correlation is diffracted at a different spatial position. This way, at the CCD, it is possible to see spatially separated rings (Fig 2). This allows to quantify the number of independent experimental spectral windows the Fourier synthesizer can control SLM.

The axicon was designed to guarantee around 10 independent spectral windows (Sec. I): this number is calculated considering a given beam waist and central wavelength, and ideal blaze profile and optical components. The tests reported in Fig. 2b show that it is indeed possible to resolve at least 10 different circles by the procedure described

above, encoding a linear blazed grating in the hologram. We expect that by adjusting the beam waist it should be possible to push the effective number of spectral windows above 10, even for a narrowband source like the titanium-sapphire laser used in this work.

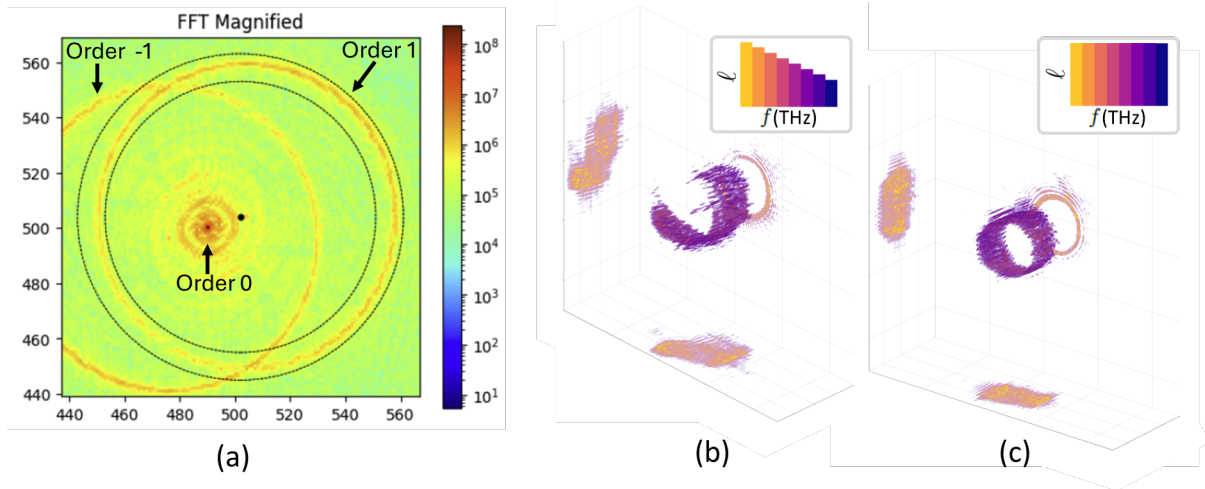


FIG. 1. **Reconstruction of the LS isosurface.** The angle between the arms of the interferometer is decisive to the proper reconstruction of the LS. It directly impacts the FFT (a), which is used to reconstruct the intensity profile of the LS, used to plot the LS isosurface, (b) and (c). (b) Shows a LS isosurface with linear space-time correlation, and (c) shows a torus isosurface, a structure where the same topological charge is applied to all frequencies to create the spatio-spectral correlation. In (b) and (c) ℓ represents the topological charges and f the laser frequencies.

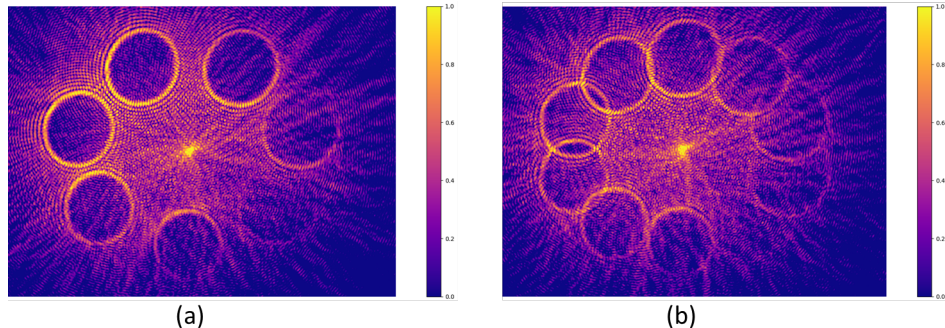


FIG. 2. **Experimental calibration of the axicon and SLM.** To test the control of the spectral windows created with the axicon grating, in addition to the topological charges applied to each window, a linear diffraction grating was added to the hologram displayed at the SLM. This allows to quantify the control over the spectral independent points (7 (a) and 10 (b)) with the SLM.

IV. EXPERIMENTAL ANGLE EXTRACTION OF LIGHT SPRING INTENSITY PROFILE

To experimentally measure v_{og} , two quantities need to be extracted: the angle variation of the LS hotspot ($\frac{\partial\alpha(t)}{\partial t}$) and the LS radius (r_{LS}) (Eq. 2).

The angle variation is measured, taking into account the LS hotspot. This means that the angle extracted is the clockwise angle on the x-axis (Fig. 3a) of the LS, considering its weighted intensity hotspot (Fig. 3b). The radius extraction is done considering the central ℓ applied to create the LS. This value is used to calculate both the experimental v_{og} (Eq. 2) and the programmed v_{og} (Eq. 3).

Since the v_{og} tunability is explored in this work via the manipulation of the LS radius, the $\frac{\partial\omega}{\partial l}$, and therefore the $\frac{\partial\alpha(t)}{\partial t}$ should be the same to all topological charges used to generate the LS. This can be seen in Fig. 3b, the range of topological charges used to synthesize the LS is different, but the experimentally measured slope is approximately the same.

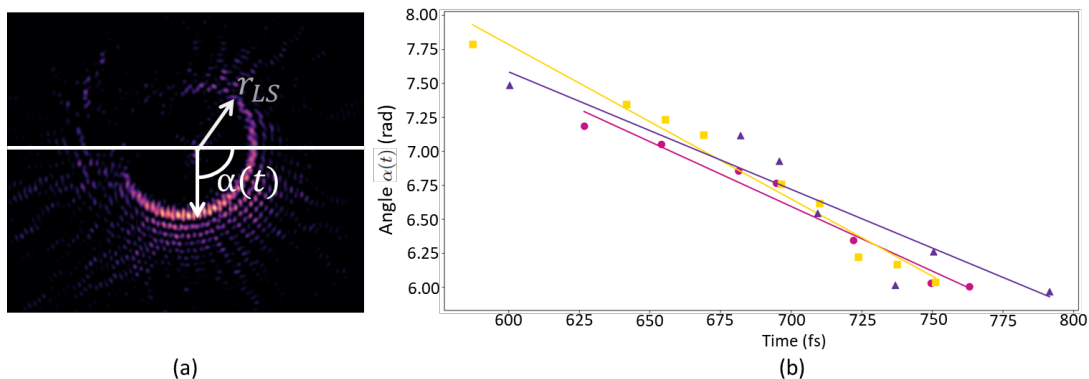


FIG. 3. **Experimental measurement of the intensity hotspot rotation as the LS propagates.** To experimentally measure the v_{og} , the angle ($\alpha(t)$) variation of the LS intensity hotspot (a) is tracked as the helical wave packet propagates (b). In (b), the pink circle, yellow square, and purple triangle represent the measured angles for topological charges of 60, 80, and 100, respectively, while the lines represent the linear fit of the measured angles.

V. LIGHT SPRING SIMULATIONS

To simulate the LS propagation, a simulation box was defined by a $2D$ window with a given $X - Y$ dimension, discretized into $M = 100$ pixels, with a time interval corresponding to the LS propagation through that window. The time interval was divided into an integer number of N steps (typically around 1200), each time step determined by an $M \times M$ matrix of the LS cross-section at that corresponding time. This results in an $M \times M \times N$ complex matrix of the calculated electric field of the LS.

The $X - Y$ dimension of the window and time interval were adjusted according to the beam waist and the v_{og} value to ensure an accurate and efficient simulation of the experimental conditions. Each simulated LS was defined by the frequency bandwidth (defined by a low-end and high-end value), the applied topological charges (defined by a low-end integer value and a high-end integer value), and the number of spectral windows (an integer value determined by the spatio-spectral linear coupling that generates the LS).

The LS was generated from the superposition of simulated Bessel-Gauss (BG) beams with a fixed beam waist. For each time step, the cross-sectional electric field was calculated by the sum of the BG electric fields corresponding to the input parameters used to create the LS, according to Eq. 4 from [2]. After the LS was simulated, the v_{og} and the LS radius were extracted from it and compared with the measured experimental values.

VI. SUPERRADIANT PLASMA MECHANISM SIMULATIONS DESCRIPTION

The simulations of the interaction between the light springs and the overdense plasma were performed using the particle-in-cell (PIC) code Osiris [3] with the radiation diagnostic tool Radio [4] turned on.

To simulate the LS in the PIC code, we decompose the field into Laguerre-Gaussian (LG) modes rather than Bessel-Gauss (BG) modes. This decision is motivated by the finite transverse size of LG modes; compared to similar BG modes, LG modes allow for significantly smaller simulation domains. This choice does not impact the final conclusions, as the underlying physical mechanism relies solely on the orbital group velocity. This velocity depends only on the radial position of the intensity maximum and the rotation speed, which is determined by the frequency-dependent azimuthal mode indices.

The LS propagates in the positive z direction and is linearly polarized in the y direction. It is composed of 31 Laguerre-Gaussian (LG) modes with frequencies evenly spaced in the range $\omega \in [0.598; 0.658]\omega_p$ (average frequency $\omega_0 = 0.628\omega_p$ with spacing $\Delta\omega = 0.002\omega_p$). The radial index of the LG modes is set to $p = 0$ and the azimuthal index is set to achieve the desired orbital group velocity: consecutive LG modes differ by $\Delta\ell = 1$ and the average index is ℓ_0 . The parameters used can be seen in Table I. Each LG mode has a spot size of $100c/\omega_p$, focuses at the origin, has a longitudinal squared sine envelope with rise and fall lengths of $500c/\omega_p$ and a flat length of $10000c/\omega_p$, and equal normalized peak wave vector amplitude. These parameters allow both LS to have the same energy.

$v_{og} (c)$	ℓ_0	ℓ_{\min}	ℓ_{\max}	$r_{LS} (c/\omega_p)$	$ E _{\max} (m_e c \omega_p e^{-1})$
0.60	18	3	33	300.0	0.161
2.00	200	185	215	1000.0	0.167

TABLE I. Parameters used for each LS used in the simulations.

The intensity of each Laguerre-Gaussian mode is given by

$$|E_y(z, r, t)| = E_0 \frac{w_0}{w(z)} \left(\frac{r\sqrt{2}}{w(z)} \right)^{|\ell|} \exp\left(\frac{-r^2}{w^2(z)}\right), \quad (6)$$

where $z_R = \pi w_0^2/\lambda_0$ and $w(z) = w_0 \sqrt{1 + (z/z_R)^2}$. The beam divergence angle is then given by

$$\theta_{BD} = \lim_{z \rightarrow \infty} \arctan \frac{r_{\max}(z)}{z} = \arctan \frac{\sqrt{\ell_0} \lambda_0}{\sqrt{2} \pi w_0} \quad (7)$$

where $r_{\max}(z)$ satisfies $(\partial_r |E_y|)_{r=r_{\max}} = 0$.

The electron plasma slab ($m/q = -1$) has a density of $n_0 = 1$ and is confined in the z direction between $z = \pm 10.0c/\omega_p$.

The radiation from 20% of the particles is captured in a spherical detector positioned in the far field in the negative z direction, at $z = -10^6 c/\omega_p$. It captures the radiation up to 2.2 rad in all directions with respect to the negative z axis between $t = -500\omega_p^{-1}$ and $t = 13000\omega_p^{-1}$. It is composed of 160 cells in each angular direction and 4000 cells in the temporal domain.

The PIC simulation box ranges from $z = -30.0c/\omega_p$ to $z = 30.0c/\omega_p$, with $n_z = 115$ cells, and from $x, y = -1200.0c/\omega_p$ to $x, y = 1200.0c/\omega_p$, with $n_{x,y} = 400$ cells. Each cell contains 4 simulation particles. The simulation is run from $t = 0.0\omega_p^{-1}$ to $t = 12000.0\omega_p^{-1}$ in steps $dt = 0.5\omega_p^{-1}$. Both the electromagnetic fields and the particles have open boundary conditions in all spatial dimensions.

Using a normalized plasma density of $n_0 = 2.824 \times 10^{21} \text{ cm}^{-3}$, both LS have a wavelength of $\lambda_0 = 1 \mu\text{m}$, a spot size of $w_0 = 10\mu\text{m}$, a flat temporal duration of $\tau \approx 3335.6 \text{ fs}$ and a total energy of 0.669 J .

VII. SUPERRADIANT PLASMA MECHANISM: SIMULATION RESULTS

A. Wavefront picture

To better understand the quasiparticle picture, let us consider that the radiation is generated by azimuthally evenly spaced emitters at the LS radius, r_{LS} , radiating unipolar spherical waves with a delay given by $\Delta t = r_{LS} \Delta\alpha / v_{og}$, where $\Delta\alpha$ is the azimuthal spacing of the emitters. The wavefronts from each wave will appear as a line in the detector, as seen in Figures 4(b) and (c) of the main text. For the superluminal case, it is clear that these lines superimpose each other at the Cherenkov angle, creating the characteristic cardioid shape. The discrepancies between the theoretical lines and the simulated intensity arise from the fact that the radiation is not composed by a single peaked wavefront but a more smoothed out wave, which blurs the intensity on the detector.

To derive the lines on the detector, consider a spherical detector with radius R_d centered at the origin is described in spherical coordinates (θ, ϕ) as

$$\begin{cases} z_d = R_d \sin \theta \cos \phi, \\ x_d = R_d \sin \theta \sin \phi, \\ y_d = R_d \cos \theta \end{cases}$$

A spherical wave composed by a single wavefront is radiated by an emitter located at $\mathbf{r} = (z_0, x_0, y_0)$ at $t = 0$. If this wavefront hits the detector at a time t , then the intersection is given by:

$$\theta(\phi) = \arctan \left(\frac{y_0^2 A \pm B \sqrt{y_0^2 C}}{y_0 (AB \mp \sqrt{y_0^2 C})} \right),$$

where

$$\begin{aligned} A &= R_d^2 + |\mathbf{r}|^2 - c^2 t^2, \\ B &= z_0 \cos \phi + x_0 \sin \phi, \\ C &= 2R_d^2 y_0^2 + 2c^2 t^2 (R_d^2 + |\mathbf{r}|^2) - c^4 t^4 - R_d^4 - |\mathbf{r}|^4 - 2R_d^2 \left((x_0^2 - z_0^2) \cos 2\phi - 2x_0 z_0 \sin 2\phi \right). \end{aligned}$$

This equation was used to create Fig.4b and c in the main text and the movie by considering 600 emitters located at $\mathbf{r}_i = (z_0, r_{LS} \cos \alpha_i, r_{LS} \sin \alpha_i)$ emitting at $t_i = r_{LS} \alpha_i / v_{og}$, with α_i uniformly distributed in the range $[0, 6\pi]$.

B. Spectral phase

To assess the orbital angular momentum content of the radiation coming from the LS interaction with the plasma, the spectral intensity and phase were retrieved from the electric field parallel to the LS polarization direction pattern in the superluminal case. Figure 4 (a) portrays the spectrum at the Cherenkov angle as a function of the frequency and angle in the $\theta - \phi$ plane. For each n^{th} harmonic, the phase wraps around $n - 1$ times angularly, corresponding to a azimuthal index n . The shift -1 comes from the polarization of the radiation. The relationship between azimuthal index and harmonic number is seen in Fig. 4 (b). After the $\sim 25^{\text{th}}$ harmonic, the index ℓ is no longer described by the previous equation. This is explained by the intensity of these harmonics quickly dropping as they are no longer inside the coherence frequency range of the emission.

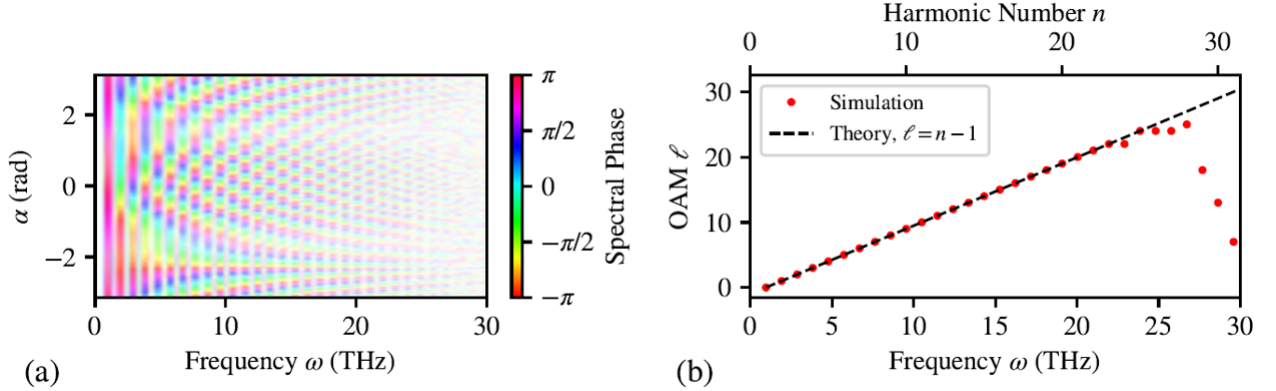


FIG. 4. **Spectral Phase and Orbital Angular Momentum (OAM) analysis** (a) Color map showing the spectral phase distribution as a function of frequency ω and angle α in the $\theta - \phi$ detector plane at the Cherenkov angle. At each harmonic, the phase wraps around an integer number of times around the axis. (b) Extracted OAM topological charge ℓ (red dots) plotted versus frequency ω and the corresponding harmonic number n (top axis).

C. Temporal description of the train of unipolar pulses

The temporal evolution of the light burst in the superluminal case, Fig. 4f of the main text, is here further analyzed. The 3 most prominent peaks were fitted to Lorentzian functions given by

$$f(t) = A_0 \frac{(\Gamma/2)^2}{(t - t_0)^2 + (\Gamma/2)^2}.$$

The results are shown in Table II. All have a similar temporal duration of $\approx 24 fs$ and are spaced by $\approx 1047 fs$, exactly the temporal pitch of the light spring $2\pi r_{LS} / v_{og} = 2\pi \times (100 \mu m) / (2 \times 0.299 \mu m / fs) \approx 1047.92 fs$.

D. Efficiency estimation

To estimate the efficiency of the conversion process, the electric field at a perpendicular slice to the plasma near the surface of the plasma was captured in two simulations: without and with the plasma. The first one captured the

Peak	A_0	Γ (fs)	t_0 (fs)
1	0.09	23.07	651.38
2	0.92	24.31	1698.38
3	0.74	24.13	2745.76

TABLE II. Lorentzian fitting parameters for the peaks in Fig.4f of main text.

incident radiation while the difference between the second and the first captured the reflected radiation. This data was saved for one full LS rotation period ($\approx 1047fs$).

The details of the analysis are plotted in Figures 5(a) and (b). The first and second plots of the top row of each sub figure represent the total integrated energy density over the detector plane for the first and second simulations respectively. The third plots show the total integrated energy density correspondent to the frequencies of the THz radiation we are interested in. For completeness, the radiation correspondent to the second harmonic was also captured and the integrated energies are plotted in the fourth plots. The bottom plots show the total integrated power on all the detector, shown either over time and as the total spectrum. Regarding the plots over time, the curves for the signal and the second harmonic were obtained by reverse Fourier transforming the spectrum and integrating the result over the detector plane.

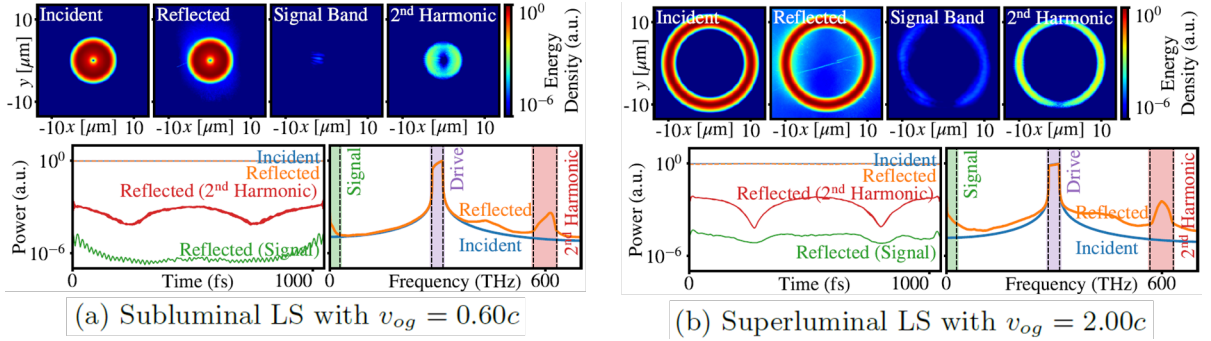


FIG. 5. Efficiency of the 3 main components of the reflected radiation captured on the grid of the simulation close to the plasma surface.

By integrating the power on the drive frequency range in the incident spectrum and the drive, signal and second harmonic frequency range in the reflected spectrum, the efficiencies for each of the reflected components can be obtained. The results are portrayed in Table III.

v_{og} (c)	Pure reflection (%)	Signal (%)	2 nd Harmonic (%)
0.60	99.32	0.01	0.06
2.00	93.68	0.06	0.34

TABLE III. Efficiency of the 3 main components of the reflected radiation captured on the grid of the simulation close to the plasma surface.

-
- [1] H. E. Kondakci and A. F. Abouraddy, “Optical space-time wave packets having arbitrary group velocities in free space,” *Nature Communications* **10** (2019).
- [2] H. Zhang, J. Zeng, X. Lu, Z. Wang, C. Zhao, and Y. Cai, “Review on fractional vortex beam,” *Nanophotonics* **11**, 241–273 (2021).
- [3] R. A. Fonseca *et al.*, “OSIRIS: A three-dimensional, fully relativistic particle-in-cell code for modeling plasma-based accelerators,” in *Computational Science — ICCS 2002*, edited by P. M. A. Sloot *et al.* (Springer, Berlin, Heidelberg, 2002), pp. 342–351.
- [4] M. Pardal *et al.*, “RaDiO: An efficient spatiotemporal radiation diagnostic for particle-in-cell codes,” *Computer Physics Communications* **285**, 108634 (2023).

